



Article

Impact of Weather Factors on Unmanned Aerial Vehicles' Wireless Communications

Lalan Mishra * and Naima Kaabouch *

Artificial Intelligence Research Center, University of North Dakota, Grand Forks, ND 58202, USA

* Correspondence: lalan.mishra@und.edu (L.M.); naima.kaabouch@und.edu (N.K.)

Abstract: As the applications of unmanned aerial vehicles (UAV) expand, reliable communication between UAVs and ground control stations is crucial for successful missions. However, adverse weather conditions caused by atmospheric gases, clouds, fog, rain, and turbulence pose challenges by degrading communication signals. Although, some recent studies have explored the nature of signal attenuation caused by atmospheric weather variations, studies that compare the attenuation from various weather conditions and analyze the effect on available bandwidth are missing. This work aimed to address this research gap by thoroughly investigating the impact of atmospheric weather conditions on the bandwidth available for UAV communications. Quantitative and qualitative performance analyses were performed for various weather conditions using metrics such as attenuation and the bit error rate of the received signals associated with different modulation schemes and frequencies, using a linearly segmented attenuation model. The results indicate that atmospheric gases and clouds/fog affect wireless signal propagation; however, the effect of rain on the propagation distances and operating frequencies considered in this study was the most severe. Based on the influence of power transmission, operating frequency, modulation schemes, distance, and adverse weather conditions on the bit error rate and bandwidth suboptimization, we propose an algorithm to select the maximum operating frequency for reliable UAV link operation.

Keywords: UAV; UAS; ground control station (GCS); command and control (C2); attenuation; bit error rate (BER); rain rate



Academic Editor: Stefano Rinaldi

Received: 11 November 2024

Revised: 25 December 2024

Accepted: 1 January 2025

Published: 8 January 2025

Citation: Mishra, L.; Kaabouch, N. Impact of Weather Factors on Unmanned Aerial Vehicles' Wireless Communications. *Future Internet* **2025**, *17*, 27. <https://doi.org/10.3390/fi17010027>

Copyright: © 2025 by the authors. Licensee MDPI, Basel, Switzerland. This article is an open access article distributed under the terms and conditions of the Creative Commons Attribution (CC BY) license (<https://creativecommons.org/licenses/by/4.0/>).

1. Introduction

The UAV market space is growing rapidly [1,2]; therefore, ensuring wireless communication reliability when establishing a dependable wireless link under all operating conditions is of utmost importance. Atmospheric weather conditions are important factors affecting the operational reliability of wireless links. Varying degrees of atmospheric weather conditions combined with wireless channel characteristics affect wireless signals differently, and their effects could lead to inoperable conditions of the wireless link at a given operating frequency [3,4]. However, critical UAV operations require fully reliable wireless communication under all weather conditions [5]. Various weather conditions can affect signals between ground control stations (GCSs) and UAVs, leading to signal deformation caused by attenuation, polarization, phase shift, and propagation delays, thereby reducing communication coverage [6–8]. Empirical data reveal that the effect is more pronounced for frequencies greater than 20 GHz because of the decrease in wavelength [9].

Most studies have concentrated primarily on one weather aspect, such as rain, and its effect on the attenuation of frequency bands at 28 GHz, 30 GHz, and 60 GHz. For

example, the authors of [9] studied the impact of rainfall on autonomous vehicles and reported that the millimeter wave (mmWave) radar detection range was reduced by up to 45% under severe rainfall conditions. The authors of [10] provided an overview of the effects of atmospheric change on mmWave propagation, specifically the collective attenuation caused by rain, water vapor, dry air, and fog. They concluded that various weather conditions affect the signal propagation. For example, a higher humidity level causes greater path loss owing to water vapor attenuation. The authors of [11] performed real-world experiments to investigate the impact of rain on mmWave propagation at 26 GHz. They collected measurements for one year with 1-min intervals and concluded that rain attenuation was 26.2 dB/km on average, and the total rain attenuation over 1.3 km was 34 dB. Rainfall rate and raindrop size related studies were also reported by the authors of [12–14], who concluded that higher rainfall rates and larger raindrops lead to higher scattering and absorption.

Other researchers focused on other aspects of weather-centric issues that affect wireless signal propagation as well as basic channel attenuation characteristics. For example, the authors of [12,15] analyzed rain-induced phase changes in orthogonal frequency division multiplexing (OFDM) signals and proposed a pre-demodulation phase compensation method to improve system performance. The authors of [13] considered various weather conditions to evaluate the impact on the channel capacity for a given bandwidth while considering a fixed wireless link. They also evaluated the impact of wind due to vibrations in the antenna structure. The authors concluded that rain-induced attenuation was the dominant factor. The effects of wind and rain were also considered by the authors of [14] with similar observations. Other researchers focused on analyzing the channel capacity under different weather conditions [13,15].

Artificial intelligence (AI) and machine learning-based (ML) techniques have been researched by several researchers for UAV channel modeling. The authors in [16] used the deep neural networks-based approach for channel modeling and introduced a system combining multiple Gaussian–Bernoulli restricted Boltzmann machines for dimensionality reduction and initial training. Their implementation was integrated with a deep neural network based on autoencoders. Channel modeling was also studied by the authors of [17] for mountainous terrain. They applied the ray-tracing method to reconstruct the propagation scenario and then acquired the wireless channel data at 3.5 GHz, 4.9 GHz, 28 GHz, and 38 GHz bands in mountainous scenarios. Important statistical properties, such as the power delay profile, Rician K-factor, path loss, and root mean square delay spread, were captured and analyzed. Channel characteristics were also analyzed.

A noticeable gap is the lack of studies that comprehensively analyze the most effective weather conditions for signal attenuation and bandwidth availability. Most studies have concentrated primarily on one weather aspect, such as rain, and its effect on the attenuation of frequency bands at 28 GHz, 30 GHz, and 60 GHz. Additionally, no prior studies have conducted comprehensive analyses of the effects of the most important weather conditions on various UAV communication frequencies, power transmissions, modulation schemes, and distances. These research gaps highlight the need for comprehensive studies to evaluate the effects of various combined meteorological conditions on signal attenuation and bandwidth availability. Therefore, this study aims to fill this gap by investigating the impact of the most critical weather conditions, such as atmospheric gases, cloud/fog, and rain, on UAV-to-GCS communication, covering a wide range of modulation schemes, distances, and other important variables.

The main contributions of this paper are as follows:

- A simplified uniformly distributed multi-segment model of the link to compute weather-specific attenuation and its comparison with non-linear model of the link.

- The impact of weather-related factors affecting bandwidth availability.
- A methodology for modeling the impact of adverse weather conditions on bandwidth availability and determining the new maximum operating frequency under a specified channel model and set of operating parameters.
- A methodology to determine permissible relative speed to allow UAV operation under a given bit error rate (BER) constraint.

The remainder of this paper is organized as follows: Section 2 describes the methodology in terms of the mathematical and system models used in this study. Section 3 details the results and comprehensively analyzes the various results obtained from the mathematical models. Section 4 provides this study’s conclusions and future work.

2. Methodology

This study aims to investigate the impact of weather factors on wireless signal propagation between a GCS and a UAV. These factors are atmospheric gases, clouds and fog, and rain. The effects of these factors were evaluated using attenuation and BER as key metrics to analyze the results both qualitatively and quantitatively, using functions of several parameters, including temperature, pressure, humidity, propagation distance, path elevation angle, geographic elevation, and operating frequencies.

Figure 1 illustrates the weather dependent characteristics of the atmosphere and related effects on propagating wireless signals.

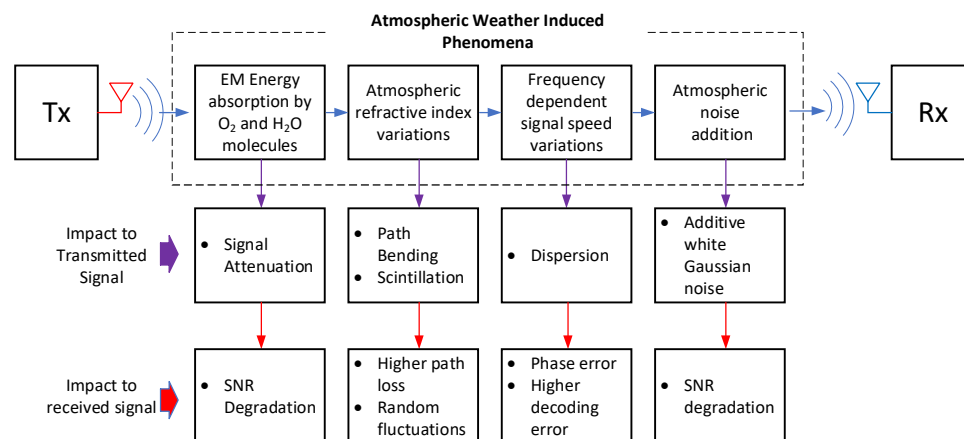


Figure 1. Atmospheric phenomena on the path of signal propagation.

Weather-induced phenomena can be primarily classified into four categories: attenuation leading to signal power reduction and signal to noise ratio (SNR) degradation, path bending and elongation due to refractive index changes, dispersion due to frequency-dependent signal speed variations, and additive noise-induced SNR degradation. Assuming a relatively short distance (maximum 2 km) and the line-of-sight communication considered in this study, only attenuation and additive noise-related considerations are essential.

2.1. Mathematical Models

In the context of UAV communications, slant path propagation represents a more generalized case of signal propagation. The variability in temperature, pressure, and water vapor concentration due to altitude/height changes necessitates that for slant path propagation, attenuation must be computed over multiple path segments such that each segment can be assumed to have constant values for these variables. Both linear and nonlinear path segmentation methodologies may be used for this investigation. While linear path segmentation approach is adequately suitable for communications associated with short distances (<2 km), as applicable in this case, the nonlinear path segmentation

approach described in [6] is more appropriate for very long-distance communications, primarily involving satellites.

Figure 2 depicts linearly and non-linearly segmented path models for the computation of attenuation resulting from atmospheric weather conditions. Figure 2a shows the linear model where the UAV height is split into N uniformly distributed equal length segments. Figure 2b illustrates the non-linear model. In this model, the height is split into M segments of non-linear lengths, per [6].

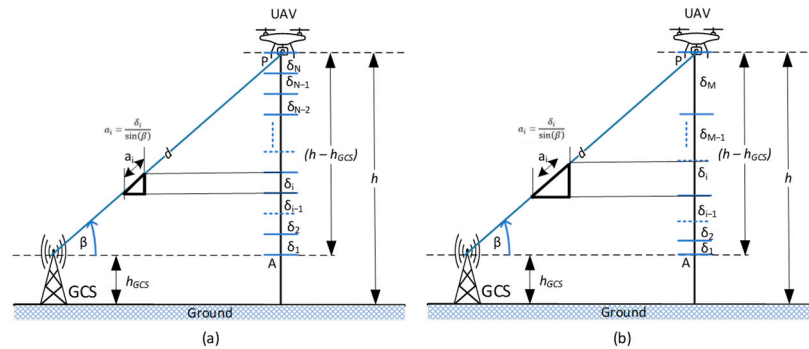


Figure 2. Illustration of path segmentation approaches: (a) demonstrates linear segmentation with N path segments of equal lengths, and (b) illustrates nonlinear segments with M path segments of nonlinearly increasing lengths.

Both models follow the approach of piecewise computation of attenuation for the associated propagation path segments over distance d . Effective attenuation for the entire path of propagation is obtained by summation of piecewise computed attenuations.

Accordingly, the generic expression for the total attenuation along the slant path is given by

$$A_{\text{slant}} = \frac{1}{\sin(\beta)} \sum_{i=1}^{i=N,M} \delta_i \quad (1)$$

where β is the angle of elevation, δ_i is the path length corresponding to the i_{th} height segment, γ_i is the corresponding attenuation, and N , and M correspond to the highest values of the path segment index for linearly and non-linearly segmented path models, respectively.

We validated our decision to select the simpler linearly segmented path model by comparing the attenuation results obtained from the two models and finding a negligible difference between the two.

Figure 3 illustrates the comparison of atmospheric attenuation between a linear and a non-linear atmospheric model for a propagation distance of 2000 m (6500 ft), UAV height of 400 m, and carrier frequencies of 1, 5, and 10 GHz, at standard atmospheric conditions.

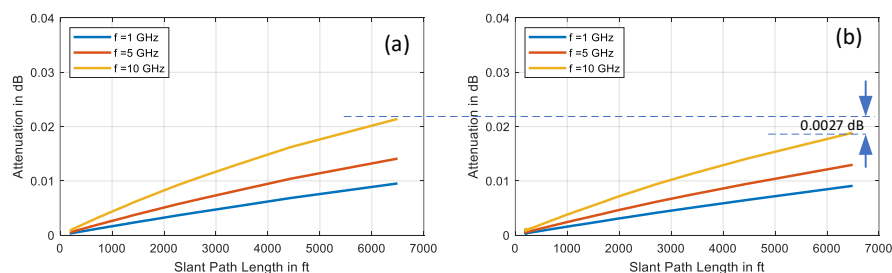


Figure 3. Comparison of atmospheric attenuation for linear and nonlinear path segmentations: (a) represents the attenuation corresponding to the linear model, and (b) illustrates the attenuation corresponding to the non-linear model, operating at standard atmospheric conditions: elevation at mean-sea level, $T = 25^\circ\text{C}$, $p = 1\text{ Atm}$, liquid water density $= 7.5\text{ g/m}^3$.

Figure 3a represents the attenuation resulting from a linearly segmented model, whereas Figure 3b depicts the results obtained from the non-linear model. A very small difference of 0.0027 dB at the highest points of attenuation between the two models suggests that the use of the linear model is closely matched with the non-linear model over small distances.

The attenuation γ_i is scaled according to the specific attenuation, which represents the attenuation for a path length of 1 km. Further, the specific attenuation is defined by different equations for gases, clouds/fog, and rain due to the variations in their attenuation characteristics [6–8]. Additionally, atmospheric parameters, such as temperature, pressure and humidity, which vary due to variations in height, affect the attenuation. To ensure the accuracy of the computational model, we applied necessary corrections to the values of the atmospheric parameters for each segment of the height [6].

2.1.1. Attenuation Due to Atmospheric Gases

Nitrogen, oxygen, argon, and carbon dioxide represent the main constituents of the atmosphere. Table 1 shows their percentage distribution for four different concentrations of water vapor [18].

Table 1. Major atmospheric gases, including water vapor.

Water Vapor	Nitrogen	Oxygen	Argon
1%	77.30%	20.70%	0.92%
2%	76.52%	20.53%	0.91%
3%	75.74%	20.32%	0.90%
4%	74.96%	20.11%	0.89%

The specific attention due to the atmospheric gases γ_g , is given by [6]

$$\gamma_g = 0.1820 \times f \left(N''_{\text{Oxygen}}(f) + N''_{\text{Water vapor}}(f) \right) \quad (2)$$

where f is the frequency and $N''_{\text{Oxygen}}(f)$ and $N''_{\text{WaterVapor}}(f)$ are the imaginary parts of the frequency-dependent complex refractivity of oxygen and water vapor, respectively.

Attenuation due to atmospheric gases along a specified line-of-sight path is subsequently determined by substituting the value of γ_i in Equation (1) with the value of γ_g for the specific path segment.

2.1.2. Attenuation Due to Clouds and Fog

Wireless signal attenuation as it propagates through clouds or fog is mainly caused by dispersion and absorption [19], which result from interactions with their constituent particles. These particles, which can range in size from tens to several hundred micrometers [20] and may vary in composition, may consist of water, ice, or a combination of both particles. The absorption and dispersion properties in clouds and fog differ significantly from those of water vapor in the atmosphere, primarily due to the distinct nature of the present particles. These differences in particle composition are key factors influencing the signal attenuation in such environments. As such, attenuation due to clouds and fog is governed by a different model than the one used for gases, and is given by [7]:

$$\gamma_c = K_l(f, T)\rho_l \quad (3)$$

where γ_c is the specific attenuation of cloud, K_l is the cloud liquid water specific attenuation coefficient, f is the operating frequency, T is the cloud liquid water temperature, and ρ_l is the liquid water density of cloud/fog.

Further, the value of $K_L(f)$ is given by

$$K_L(f) = K_I(f, T) \cdot \left(A_1 e^{-\frac{(f-f_1)^2}{\sigma_1}} + A_2 e^{-\frac{(f-f_2)^2}{\sigma_2}} + A_3 \right) \quad (4)$$

where $A_1 = 0.1522$, $A_2 = 11.51$, $A_3 = -10.4912$, $f_1 = -23.9589$, $f_2 = 219.2096$, $\sigma_1 = 3.2991 \times 10^3$, and $\sigma_2 = 2.7595 \times 10^6$.

Attenuation resulting from clouds/fog along a specified line-of-sight path is subsequently determined by substituting the value of γ_i in Equation (1) with the value of γ_c for the specific path segment.

2.1.3. Attenuation Due to Rain

The specific attenuation γ_r due to rain is given by [8]:

$$\gamma_r = k \cdot R_r^\alpha \quad (5)$$

where R_r is the rain rate, and k and α are the frequency and path elevation dependent parameters, as described in Equations (2)–(5) [8].

Attenuation resulting from rain along a specified line-of-sight path is subsequently determined by substituting the value of γ_i in Equation (1) with the value of γ_r for the specific path segment.

2.1.4. Total Atmospheric Weather Attenuation

Figure 4 illustrates the attenuation arising from different weather conditions along the path of propagation.

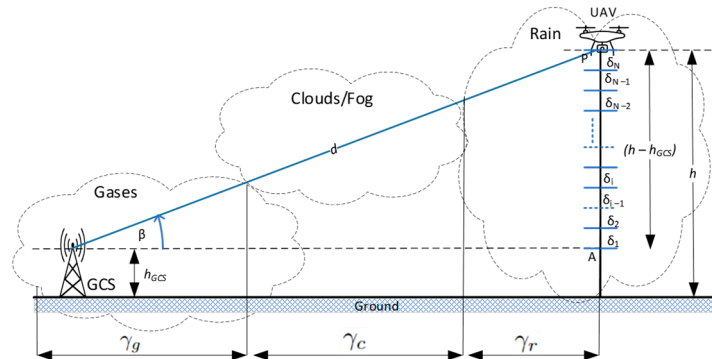


Figure 4. Attenuations along the path of propagation due to atmospheric weather variations.

Total attenuation A_{total} along the path of propagation due to atmospheric weather conditions is calculated by summing each individual attenuation due to gases, clouds and fog, and rain.

$$A_{total} = \gamma_g + \gamma_c + \gamma_r \quad (6)$$

2.1.5. BER Evaluation

In this section, we evaluate the impact of weather-induced attenuation in terms of BER performance for different weather conditions and different modulation schemes (binary phase shift keying (BPSK), quadrature phase shift keying (QPSK), 16-quadrature amplitude modulation (QAM), 64-QAM, and 256-QAM). The BER of a communication system represents the probability that a transmitted bit is received erroneously. It is influenced by various parameters, including the modulation order M , which denotes the number of distinct symbols utilized to encode the data.

We included higher order modulation schemes as the next generation command and control systems are poised to use 5G and 6G technologies. These new generations of wireless technologies are specified to use higher order modulation for more efficient use of the limited wireless spectrum, while supporting lower order modulation schemes for backward compatibility reasons.

Higher modulation orders enable the transmission of more bits per symbol, thereby increasing data rates over a given bandwidth. For instance, given a specific symbol rate over a corresponding bandwidth, 1-bit per symbol is transmitted utilizing the BPSK modulation scheme, whereas the implementation of QPSK, 16, 64, and 256-QAM facilitates the transmission of 2, 4, 6, and 8-bits per symbol, respectively. Due to the limited availability of wireless bandwidth, maximizing the number of bits per symbol is a fundamental requirement in all wireless communications. Consequently, although the utilization of lower modulation orders may satisfy the command and control data transmission requirements between the UAV and the GCS, considering the constraints of narrow bandwidth availability, we have incorporated higher modulation schemes in our simulations.

The utilization of higher modulation schemes renders the system more susceptible to noise and interference. This is due to tighter packing of the symbols within the in-phase and quadrature plane (IQ-plane), making the symbols more susceptible to noise, as small positional variation of the symbol within the IQ-plane increases the probability of symbol boundary crossing and hence a higher probability of symbol misinterpretation.

For BPSK and QPSK modulations, the probability of bit error (P_b) is approximated by [21] as follows:

$$P_b = Q\left(\sqrt{2\gamma_b}\right) \quad (7)$$

where $Q(\cdot)$ indicates the error function and γ_b is the SNR per bit.

For M-QAM, P_b is approximated by [21] as follows:

$$P_b = \frac{4}{\log_2 M} Q\left(\sqrt{\frac{3\bar{\gamma}_b \log_2 M}{M-1}}\right) \quad (8)$$

where M indicates the number of constellation points in the QAM array and $\bar{\gamma}_b$ represents the average SNR per bit.

SNR is a critical factor in BER computation. For a given set of operating parameters, such as power transmission, propagation distance, operating frequency, and GCS and UAV heights, experimental measurements show that propagation environments have a detrimental effect on its value at the receiver. Path loss is an important factor that governs the SNR at the receiver. Several models exist in the literature that aim to model the path loss associated with GCS-to-UAV and UAV-to-UAV communications [22–25]. Inclusion of wide variations of weather conditions are not included in these models. Therefore, to include the effect of weather conditions on the received power at the receiver, we added the attenuation caused by weather conditions to the path loss predicted by the selected path loss model. The received power P_{rx} in dB is then computed as follows:

$$P_{rx} = P_{tx} - (PL + A_{total}) \quad (9)$$

where P_{tx} , PL , and A_{total} are the power transmission, path loss, and weather-based total attenuation along the path of propagation; all in dB.

Operating bandwidth dependent noise power in dB is computed as

$$P_N = 10\log_{10}(kTB) \quad (10)$$

where k is the Boltzmann constant, T is the temperature in degree kelvin, and B is the operating bandwidth in Hz.

Accordingly, the SNR γ_b is computed as

$$\gamma_b = P_{rx} - P_N \tag{11}$$

2.1.6. Effect of Mobility and Multipath Propagation on BER

In this section, we examine the effects of mobility and time-variant characteristics of the wireless channel, which negatively impact the BER performance of GCS-to-UAV wireless communications. Accordingly, we develop a mathematical model to compute effective BER after modifying the computed SNR based on a static channel model.

For this modeling, we assume OFDM based multi-carrier wireless communication between the GCS and the UAV, since it is a widely adopted modulation scheme due to its superior spectral efficiency. Both cellular and Wi-Fi communication networks, utilized for UAV command and control, employ this modulation scheme.

The complex envelope of the transmitted OFDM symbol $s(t)$, based on N sub-carriers, is given by [26] as follows:

$$s(t) = \left(\sum_{m=0}^{N-1} a_m e^{j2\pi \frac{m}{T} t} \right) e^{j\theta(t)} \tag{12}$$

where a_m is the data symbol that modulates the m^{th} sub-carrier at frequency m/T over the symbol period T , and $\theta(t)$ is a time varying phase resulting from the carrier offset between the transmitter and the receiver.

Based on different scenarios, a multitude of UAV channel models have been studied [17,24,27–29]. A general approach of channel modeling is to conduct a channel impulse response-based data collection campaign for a given region of interest, followed by statistical analysis and curve fitting to derive an empirical model.

Figure 5 illustrates a time-variant generic wireless channel through which the transmitted symbol $s(t)$ propagates to arrive at the receiver. The wireless channel includes different types of moving and stationary objects, with varying configurations and concentrations.

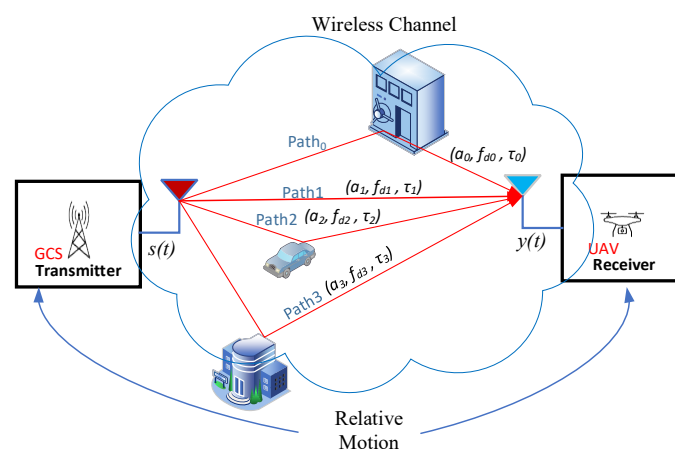


Figure 5. Illustration of mobility and multipath propagation in UAV wireless channel.

The transmitted signal $s(t)$ is reflected, refracted, and scattered by these objects. As a result, the signal propagation takes multiple paths to reach the receiver. In this illustration, only four paths are shown. However, based on the objects’ configurations and concentrations in the channel, many paths may exist.

Each path p_k , causes unique amplitude a_{p_k} , Doppler shift $f_{d_{p_k}}$, and propagation delay τ_{p_k} variations to the transmitted symbol. The received symbol $y(t)$ is the aggregation of all symbol instances arriving via different paths, plus the all-white Gaussian noise (AWGN) N_0 as applicable to the operating bandwidth B .

Figure 6 shows the mathematical formulations for the amplitude, Doppler shift, and propagation delay variations applicable to L propagation paths [30].

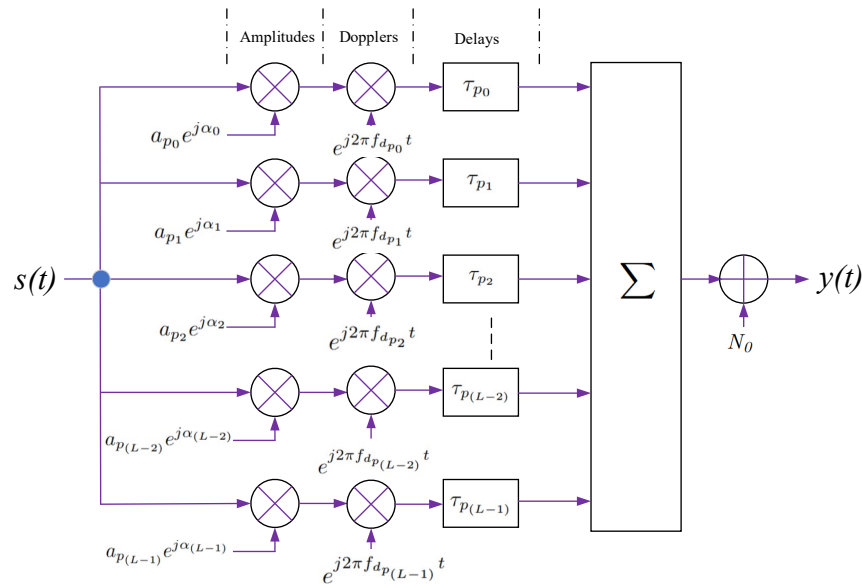


Figure 6. Multipath propagation channel and related effects.

The received symbol $y(t)$ can then be given by

$$y(t) = \left(\sum_{k=0}^{L-1} s(t) \cdot a_{p_k} e^{j\alpha_k} \cdot e^{j2\pi f_{d_{p_k}} t} \cdot \delta(t - \tau_{p_k}) \right) + N_0 \tag{13}$$

where corresponding to path p_k , $a_{p_k} e^{j\alpha_{p_k}}$, $e^{j2\pi f_{d_{p_k}} t}$ and τ_{p_k} , represent the amplitude, Doppler shift, and path delay applied to the symbol passing through it, and N_0 is the temperature and bandwidth dependent AWGN noise.

The phase variations caused by clock phase noise, Doppler shift, and propagation delays result in loss of OFDM sub-carrier orthogonality. Consequently, the OFDM sub-carriers interfere with one another. This inter sub-carrier interference (ICI) manifests as near-Gaussian noise [30], resulting in SNR degradation. As SNR degrades, link performance deteriorates due to an increase in BER.

The studies described in [26,31] investigated $y(t)$ due to the response of the multipath propagation channel on $s(t)$. The time-variant channel conditions degrade SNR due to ICI resulted noise. The SNR degradation is analyzed for two scenarios: Doppler shift, and clock phase noise. Doppler shift f_d to an applicable path is given by [28] as follows:

$$\Delta F = f_d = \frac{v_r \cdot f_c}{c} \cos(\alpha) \tag{14}$$

where v_r is the relative speed between the transmitter and the receiver, c is the speed of light, and α is the incident angle of the incoming signal.

Oscillator phase noise, associated with the transmitter and receiver, results in spectrum broadening of the clock. This broadened spectrum of the clock becomes a major cause for the loss of orthogonality in OFDM transmission. Phase noise $\theta(t)$ is governed by the

Wiener process. Accordingly, the statistical mean of $\theta(t) = 0$. The variance of the phase error is given by [26]:

$$\sigma_{\theta}^2 = 4\pi\beta \quad (15)$$

where β denotes the 3 dB linewidth of the Lorentzian power spectrum density of the oscillator. SNR degradation due to frequency offset is approximated by [31]:

$$SNR_{deg\Delta F} = \frac{10}{\ln 10} \frac{1}{3} \left(\pi N \frac{\Delta F}{R_S} \right)^2 \bar{\gamma}_b \quad (16)$$

where ΔF is the carrier offset caused by the Doppler shift, N is the number of sub-carriers, R_s is the subcarrier spacing, and γ_b is the theoretical SNR for a given channel without any frequency offset.

SNR degradation due to phase noise is approximated by [31]:

$$SNR_{deg\beta} = \frac{10}{\ln 10} \frac{11}{60} \left(4\pi N \frac{\beta}{R_S} \right) \bar{\gamma}_b \quad (17)$$

where β is the spectral linewidth caused by phase noise. Substituting ΔF in Equation (16) by the corresponding Doppler shift expression from Equation (14) and taking the maximum value of $\cos(\alpha)$, $SNR_{deg\Delta F}$ could be expressed as

$$SNR_{deg\Delta F} = \frac{10}{\ln 10} \frac{1}{3} \left(\pi N \frac{v_r f_c}{R_{Sc}} \right)^2 \bar{\gamma}_b \quad (18)$$

Expressing the total SNR degradations as the sum of $SNR_{deg\Delta F}$ and $SNR_{deg\beta}$, the effective SNR ψ can then be expressed as

$$\psi = \bar{\gamma}_b \left(1 - \frac{10}{\ln 10} \frac{1}{3} \left(\pi N \frac{v_r f_c}{R_{Sc}} \right)^2 - \frac{10}{\ln 10} \frac{11}{60} \left(4\pi N \frac{\beta}{R_S} \right) \right) \quad (19)$$

After simplifying the constant terms, ψ can be expressed as

$$\psi = \bar{\gamma}_b \left(1 - 1.448 \left(\pi N \frac{v_r f_c}{R_{Sc}} \right)^2 - 0.796 \left(4\pi N \frac{\beta}{R_S} \right) \right) \quad (20)$$

Replacing $\bar{\gamma}_b$ in Equation (8) by ψ , we obtain the degraded BER as

$$P_{b_{deg}} = \frac{4}{\log_2 M} Q \left(\sqrt{\frac{3\psi \log_2 M}{M-1}} \right) \quad (21)$$

2.2. Simulation Parameters for Atmospheric Weather Variations

The effect of atmospheric weather conditions was evaluated by varying the signal propagation distance between the GCS and the UAV, height between the UAV and the GCS, atmospheric water vapor density, atmospheric liquid water density, temperature, and rain rates across a wide range of carrier frequencies from 1 GHz to 100 GHz. Table 2 gives the list of parameters and their values used in this investigation.

The selection of weather-related parameter values aimed to capture typical annual meteorological fluctuations across various global locations.

Table 2. Weather simulation parameters.

Parameters	Values/Range of Values	Units
Temperature (T_a)	−40, −25, 25, 40	°C
Standard pressure (p_a)	1013.25	hPa
Liquid water density (lwd)	0.23, 5.75, 17.26, 23.01	g/m ³
	For fog attenuation: 0.05, 0.5, 5.0, 10	
Rain-rate (R_r)	1, 10, 50, 120	mm/h
GCS to UAV distance (d)	500, 1000, 1500, 2000	m
GCS to UAV height (h)	100, 200, 300, 400	m
Frequency (f)	1 to 100	GHz
Isotropic Transmitter power (P_{tx})	0.25, 0.75	mW
All white gaussian noise (AWGN) (N_0)	−142 to −144	dB

Globally, annual temperature fluctuations span a wide range. For 2023, the highest temperature of 53.9 °C was recorded in the Northern Hemisphere at Saratoga Spring, California, USA, while the lowest temperature was recorded as −62.7 °C in Tongulakh, Russia [32]. The selected temperature range of −40 to 40 °C is a symmetric representative interval, centered at 0.0 °C, offering a representative view of typical global temperature variations.

The water vapor density values of 0.23, 5.75, 17.26, and 23.01 g/m³ were assumed. These values correspond to 1%, 25%, 75%, and 100% relative humidity at 25 °C and 1013.25 hPa atmospheric pressure.

For the liquid water density, values of 0.05, 0.5, 5.0, and 10.0 g/m³ were used. These values correspond to cloud/fog visibility in the range of 2.5 m to 300 m.

Specifications for distance, height, operating frequencies, and transmission powers were based on commercially available UAVs, with a focus on personal applications [33]. These choices were made to reflect the characteristics of UAVs currently on the market, particularly those designed for individual consumers.

2.3. Simulation Parameters for Mobility, Doppler Shift, and SNR Degradation

The impact of mobility and resultant Doppler shift on SNR degradation was assessed through the variation of a set of key parameters as expressed in Equation (20). Assuming the maximum permissible value of BER (P_b) at 0.01, for 4, 16, 32, 64, and 256-QAM modulation schemes, we computed the corresponding values of $\bar{\gamma}_b$ using Equation (22):

$$\bar{\gamma}_b = 10 \log_{10} \frac{\left(Q^{-1} \left(\frac{P_b \log_2 M}{4} \right) \right)^2 (M - 1)}{3 \log_2 M} \quad (22)$$

where Q^{-1} is the inverse error function.

The computed values of $\bar{\gamma}_b$ thus serve as the minimum SNR thresholds for corresponding modulation schemes to maintain a BER ≤ 0.01 . We set the reference SNR at 20 dB. At this level of SNR, $P_b < 0.01$ is satisfied for all assumed modulation schemes. Degradation resulting from Doppler shift was applied to this reference SNR. The carrier frequency f_c was set to 2.4 GHz. The sub-carrier frequencies and corresponding symbol rate R_s were selected according to the fifth generation (5G) numerology [34], which is backward compatible with the fourth generation (4G) cellular communications. The number of sub-carriers were selected for quantities of 4, 16, 32, 64, and 256. SNR degradation was evaluated against the symbol rates of 15, 30, 60, and 120 Kbd/s. The relative speed to generate a Doppler shift was set in the range of 0 to 200 km/h, with 1 km/h increment. Table 3 presents the parameters utilized in this study, along with their corresponding values.

Table 3. Doppler shift and SNR degradation simulation parameters.

Parameters	Values/Range of Values	Units
Maximum permissible BER (p_b)	0.01	
QAM modulation order (M)	4, 16, 32, 64, 256	
Reference SNR	20	dB
Carrier frequency (f_c)	2.4	GHz
Number of sub-carriers (N)	4, 16, 32, 64, 256	
Symbol rate (R_s)	15, 30, 60, 120	KBd/s
Relative speed	0 to 200	km/h
Phase noise linewidth (β)	10×10^{-6}	Hz

Figure 7 illustrates the methodology employed for conducting simulations, analyzing the results, and deriving pertinent recommendations within the context of UAV operations.

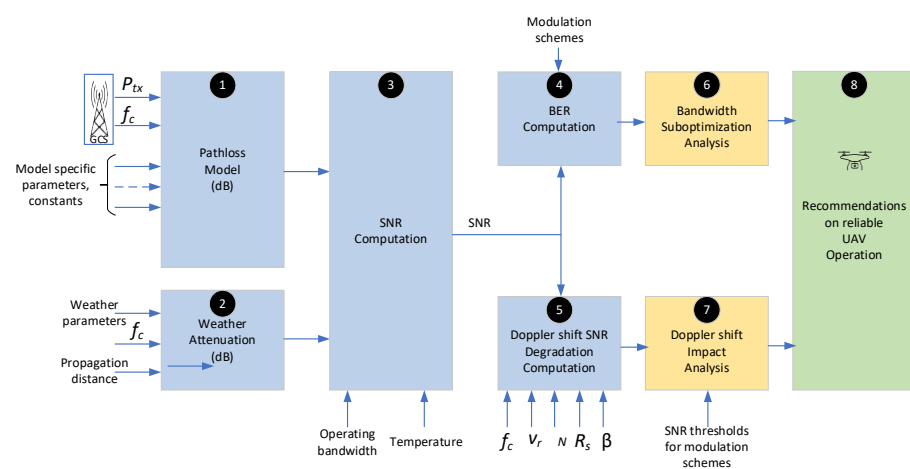


Figure 7. Simulation parameter processing and result analysis flow.

The simulations conducted include computation of ① path loss, ② weather attenuation, ③ SNR, ④ BER, and ⑤ Doppler shift caused SNR degradation. The results were used to analyze their effects on UAV operations in terms of ⑥ bandwidth suboptimization and ⑦ Doppler shift impact analysis. The analysis resulted in a set of ⑧ recommendations, which can be utilized to formulate suitable algorithms to enhance UAV operational reliability.

The path loss computation block takes the power transmission, carrier frequency, and other model-dependent parameters as inputs to compute the expected path loss at the receiver. The weather attenuation computation is carried out based on operating frequency and applicable weather parameters. The total received power is computed based on the path loss and the weather influenced attenuation. Based on the operating bandwidth and temperature, AWGN noise is computed. Subsequently, the SNR is computed as the ratio of the received power to the noise power. BER computation is performed based on the computed SNR. We apply a Doppler shift-based degradation to the SNR to evaluate the impact of mobility across different modulation schemes, symbol rates, and sub-carrier spacing.

3. Results and Discussion

3.1. Atmospheric Weather Variations

Using the previously defined parameters, we simulated different atmospheric conditions while assuming a range of frequencies and propagation distances to evaluate the effect of weather factors on wireless signal propagation and its resultant effect on the BER at the receiver. While the simulation for attenuation under different atmospheric conditions covered the range of 1 to 100 GHz, BER and bandwidth suboptimization related

simulations used the frequency range of 1 to 10 GHz, as currently available UAVs operate in this frequency range. Figures 8–10 illustrate the attenuation due to atmospheric gases, clouds/fog, and rain. Figure 11 shows the BER results for atmospheric weather conditions using different modulation schemes (BPSK, QPSK, 16-QAM, 64-QAM, and 256-QAM), and introduces two important metrics associated with the modulation schemes, maximum operating frequency (f_{max}) and reduction in maximum operating bandwidth (B_{red}). Figure 12 illustrates the effect of bandwidth suboptimization in terms of f_{max} and B_{red} due to atmospheric weather variations for two different power transmissions: 25 and 75 mW.

Figure 8a–d illustrate the influence of atmospheric gases on the signal attenuation across varying frequencies ranging from 1 GHz to 100 GHz, encompassing a broad range of operational frequencies allocated for the 5G mobile cellular networks [35]. The simulations were conducted with specific values for the associated parameters, including propagation distance, height, water vapor density, temperature, and pressure. Each figure focuses on the impact of varying one parameter at a time, while keeping the others constant.

Figure 8a exhibits the attenuation as a function of the carrier frequency and for different propagation distances (500, 1000, 1500, and 2000 m). The water vapor density, height, temperature, and pressure were maintained at 23.01 g/m³, 400 m, 25 °C, and 1013.25 hPa, respectively. As expected, a noticeable increase in attenuation was observed across all frequencies as the propagation distance increased. This phenomenon is attributed to the increased absorption of the energy of the signal along a longer path. As expected, two specific attenuation peaks are observed for each distance, one at 22 GHz and the other at 60 GHz corresponding to water and oxygen resonant absorption, respectively.

Figure 8b shows the effect of the height (100 to 400 m). The water vapor density, propagation distance, temperature, and pressure were held constant at 23.01 g/m³, 2000 m, 25 °C, and 1013.25 hPa, respectively. Interestingly, no significant increase in attenuation was observed as the height increased, presumably because of the minimal changes in atmospheric parameters (temperature, water vapor density, and pressure) across the assumed heights.

Figure 8c depicts the impact of water vapor density variation for densities ranging between 0.23 and 23.01 g/m³. The other parameters (propagation distance, height, temperature, and pressure) were maintained constant. As expected, the attenuation increased as the water vapor density increased for a local maximum of 23.01 g/m³, which corresponds to the water vapor absorption resonance frequency at 22 GHz. Although the humidity influences the attenuation peaks at 22 GHz, the peaks remain within 1 dB, a relatively insignificant value when compared with the free space path loss. For frequencies higher than 22 GHz, the attenuation decreases before exhibiting a subsequent peak at 60 GHz. However, since the 60 GHz absorption band is exclusively associated with atmospheric oxygen, the variation in water vapor density does not show any impact on the attenuation by the frequency band.

Figure 8d illustrates the effect of temperature for the four values −40, −25, 25, and 40 °C. The propagation distance, height, water vapor density, and pressure were maintained at 2000 m, 400 m, 23.01 g/m³, and 1013.25 hPa, respectively. The expected attenuation peaks at 22 GHz and 60 GHz show a marked difference in their characteristics. While the attenuation peaks corresponding to different temperatures converge at 22 GHz, at the 60 GHz oxygen absorption band, a higher attenuation was observed with lowering of temperature. Attenuations for the lowest temperature of −40 °C exceeds the attenuation at the highest temperature of 40 °C by approximately 25 dB. This is a significant increase attributed to increased absorption of electromagnetic energy by the oxygen molecules at lower temperatures.

The attenuation in the lower frequency region i.e., [0, 22 GHz], shows an increasing trend along with frequency, the magnitude stays below 1 dB. This implies that for lower

frequency UAV/GCS operation, the attenuation due to atmospheric gases is minimal. For higher frequencies, the attenuation peaks at 22 GHz and 60 GHz are due to the resonating electric and magnetic moments associated with water and oxygen molecules. Water molecules have a non-zero electric dipole moment, whereas oxygen molecules have a non-zero magnetic dipole moment. As a result, the electric and magnetic fields of the propagating electromagnetic waves interact with the water and oxygen molecules, respectively, leading to their transition to a higher energy state. Seeking a more stable state, these molecules subsequently give off a secondary emission and come back to a lower energy state. This self-perpetuating phenomenon is thus responsible for increased attenuation and secondary emission at the resonant frequencies. As the frequency increases, the energy of the EM wave increases, leading to increased energy absorption by the water and oxygen molecules within their respective absorption bands.

The increased level of electromagnetic energy absorption in these frequency bands results in higher attenuation. Increasing the propagation distance always adds to attenuation. Variation in height for a given propagation distance has negligible impact on attenuation. Other than the distance, variation in water vapor density and temperature have a noticeable impact on attenuation in the 22 and 60 GHz bands, respectively. Our study shows that temperature variation has a bigger impact (up to 25 dB) on the 60 GHz oxygen absorption attenuation. Comparatively, at 1 dB maximum variation in attenuation, the 22 GHz water absorption attenuation has a much-diminished effect. It is imperative that link budgeting between the GCS and the UAV be performed with the worst-case scenario in mind to ensure reliable operations under all conditions.

Figure 9a–c illustrate the impact of atmospheric clouds and fog on signal attenuation across the same frequencies as used in the case of gas-based attenuation. In this simulation, predetermined values for pertinent parameters associated with UAV flights were utilized. Given that clouds and fog contain larger micro-clusters of water molecules in liquid form, liquid water density was employed to quantify the amount present in a unit volume, rather than water vapor density.

Figure 9a depicts the attenuation as a function of the carrier frequency for varying propagation distances (500, 1000, 1500, and 2000 m). The liquid water density, height, temperature, and pressure were held constant at 10 g/m^3 , 400 m, $25 \text{ }^\circ\text{C}$, and 1013.25 hPa, respectively. As this figure shows, there was a noticeable increase in the attenuation of the signal as the propagation distance increased. The attenuation rose at a faster rate for frequencies under 22 GHz. Beyond this value, this rate significantly decreased. This phenomenon is attributed to the inverse relationship between frequency and wavelength, wherein higher frequencies correspond to shorter wavelengths relative to the dimensions of water droplets. Shortening of the wavelength with respect to the dimension of the water droplets results in the reduction of the scattering effect as a limiting value of the scattering coefficient. Additionally, for frequencies higher than 25 GHz, the resonant absorption by water molecules rapidly diminishes.

Figure 9b shows the impact of the UAV height on attenuation, considering heights of 100, 200, 300, and 400 m. The water vapor density, propagation distance, temperature, and pressure were maintained at 10 g/m^3 , 2000 m, $15 \text{ }^\circ\text{C}$, and 1013.25 hPa, respectively. In this instance, minimal changes in the atmospheric parameters across the assumed heights, coupled with a constant path length for all the four height values, resulted in closely matched attenuation profiles.

Figure 9c illustrates the effect of liquid water vapor density variations on signal attenuation. The other parameters, propagation distance, height, temperature, and pressure, were maintained constant at 2000 m, 400 m, $15 \text{ }^\circ\text{C}$, and 1013.25 hPa, respectively. A

corresponding increase in attenuation was observed as the water vapor density increased, in accordance with the expected result.

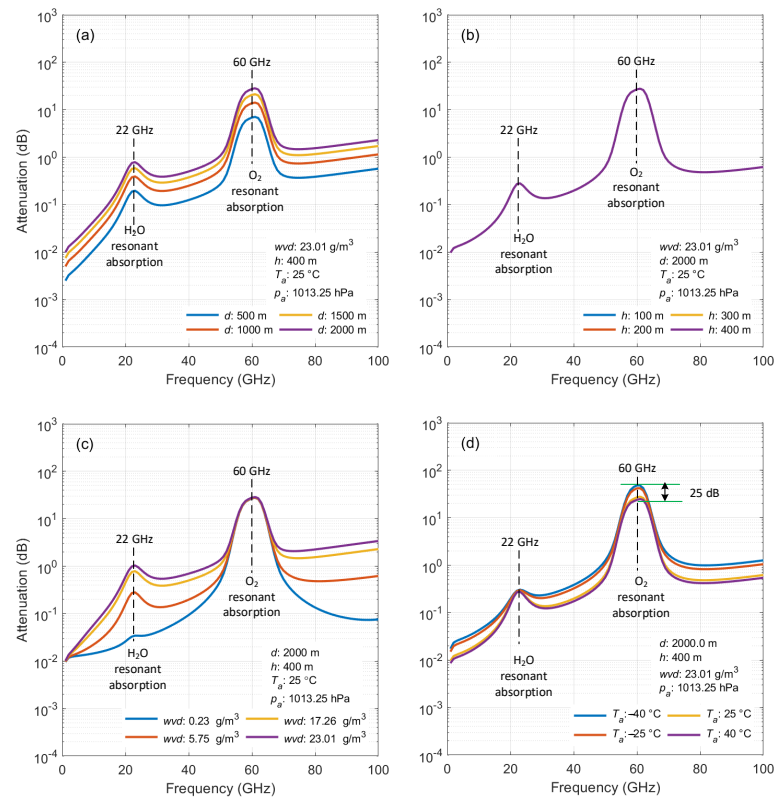


Figure 8. Effect of atmospheric gases on signal attenuation across various frequencies: (a) demonstrates the variation in attenuation for four specific distance measurements; (b) illustrates attenuation variations at different altitudes; (c) presents the influence of water vapor density variations on attenuation; (d) depicts the effect of variations in temperature.

Notably, no attenuation spike was observed for frequencies under 22 GHz band in the cloud/fog-based attenuation, as was observed in the atmospheric gas-based attenuation. This phenomenon is attributed to the larger size of the suspended water droplets resulting from the clustering of water molecules in clouds and fog due to condensation. Clustering of water molecules results in distinctive changes in the attenuation characteristics. Scattering, owing to suspended water droplets, becomes the dominant phenomenon in the ensuing attenuation [36].

Therefore, as most UAV command control systems currently operate at frequencies below 10 GHz, the maximum attenuation observed is approximately 1 dB. This attenuation is significantly lower compared to free-space path loss. Our findings also indicate that even the most severe cloud and fog conditions will result in only minimal increases in attenuation.

Figure 10 displays the results corresponding to the effect of rain on the signal attenuation over the assumed frequency range. The simulations were methodically parameterized with defined values for the critical variables: propagation distance, elevation, rain rate, ambient temperature, and atmospheric pressure.

Figure 10a provides a graphical representation of signal attenuation as influenced by carrier frequency across various propagation distances (500, 1000, 1500, and 2000 m). The conditions were standardized with a rain rate of 120 mm/h, an elevation of 400 m, a temperature of 25 °C, and an atmospheric pressure of 1013.25 hPa. Given the frequent occurrences of severe weather conditions all over the world, we selected a maximum value of rain rate

(120 mm/h, recorded in various parts of the world), to assess the maximum impact due to rain under extreme weather conditions. The results indicated a direct relationship between the increased propagation distance and the corresponding increase in signal attenuation, attributable to the combined effects of absorption and scattering phenomena.

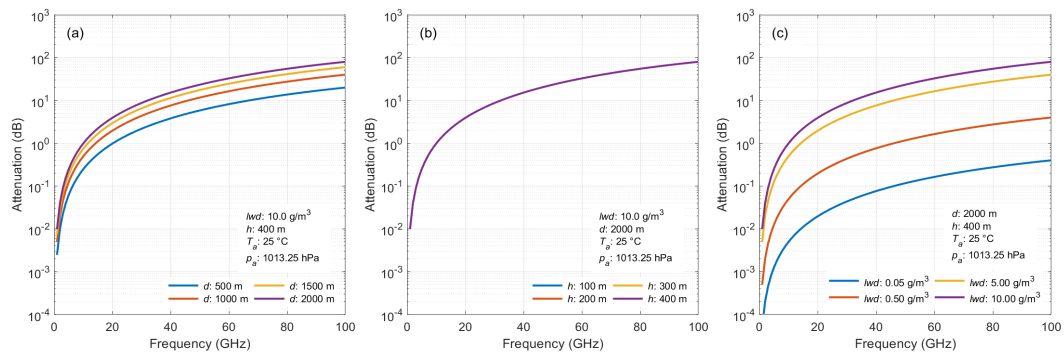


Figure 9. Impact of clouds and fog on signal attenuation across various frequencies: (a) shows how attenuation changes for four specific distance measurements; (b) illustrates attenuation variations at different altitudes; (c) presents the influence of liquid water density fluctuations on attenuation.

Absorption and scattering are governed by the wavelength of the incident signal and the size of the raindrops. Depending on the precipitation rate, raindrop diameter ranges from 0.1 to 5 mm. The signal wavelength in the frequency range of 1 to 100 GHz varies from 300 to 3 mm. When the wavelength significantly exceeds the raindrop size, Rayleigh scattering becomes the predominant mode of scattering. However, as the wavelength approaches or becomes comparable to the size of the raindrop, Mie scattering becomes the dominant mode [37,38].

As illustrated, the attenuation increased at a much faster rate in the lower frequency region, and subsequently slowed down before leveling off in the higher frequency region. This phenomenon is due to the applicability of Rayleigh and Mie scattering in different frequency regions. In the lower frequency region (<10 GHz), due to the wavelength being much larger than the raindrop diameter, Rayleigh scattering is applicable. The intensity of Rayleigh scattered signal exhibits an inverse proportionality to the fourth power of the wavelength. Consequently, increased scattering is observed at shorter wavelengths and the attenuation rises much faster. By contrast, Mie scattering does not demonstrate this pronounced dependence on wavelength reduction. As a result, the attenuation rapidly levels off in the frequency region >10 GHz.

Figure 10b illustrates the impact of varying heights, ranging from 100 to 400 m. The rain rate, propagation distance, temperature, and pressure were held constant in this case. The results show a highly consistent attenuation profile across the different heights. This consistency results from relatively unchanged atmospheric conditions and identical path lengths across the considered height range.

Figure 10c presents the effect of the precipitation intensity for rain rates of 1, 10, 50, and 120 mm/h, with the other variables held constant, as in the previous cases. As the rainfall intensity increased, there was a corresponding rise in signal attenuation. With the increase in operating frequency, although the attenuation exhibits a steep rise in the lower (<10 GHz) frequency region, the absolute value of attenuation for the highest rain rate (120.0 mm/h) remains under 50 dB. Under the assumed conditions, maximum attenuations for the rain rates of 1.0, 10.0, and 50.0 mm/h in the lower frequency range were approximately 0.1, 1, and 10 dB, respectively.

In this case, the predominance of scattering due to the larger raindrop sizes compared to the smaller particulates associated with clouds/fog leads to a more pronounced increase in attenuation.

A comparative analysis of the results for the cases of gas, clouds/fog, and rain demonstrates that, under the specified conditions, high intensity rain produces attenuation exceeding 100 dB in the 1 to 100 GHz operating range, making it the most significant atmospheric weather condition affecting UAV communications. However, for UAV/GCS operating frequencies that are under 10 GHz, the worst-case attenuation for rain approaches 50 dB. While the worst-case attenuations due to gases and clouds/fog are 0.1 dB and 1 dB, respectively. Hence, for reliable communication under all weather conditions, it is imperative that link budgeting be based on the rain-based attenuation as it far exceeds the attenuation caused by atmospheric gases and clouds/fog.

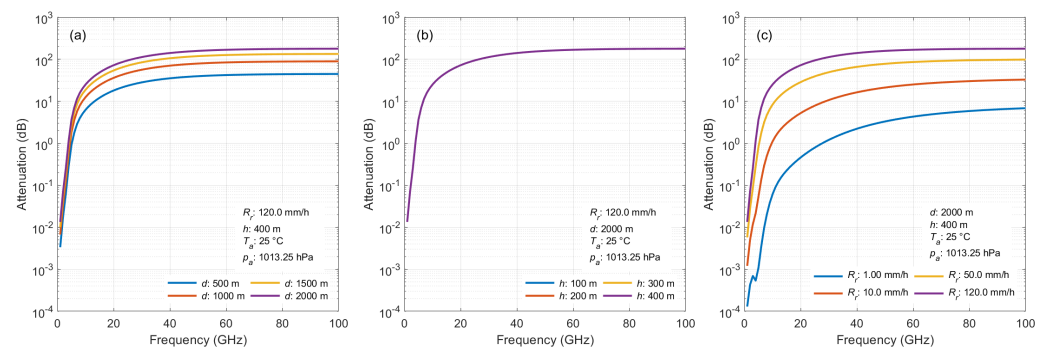


Figure 10. Rain based attenuation as a function of frequency: (a) illustrates the variation in attenuation for four distinct values of distances; (b) demonstrates the variation in attenuation for different heights; (c) depicts the effect on attenuation due to rain rate variation.

Figure 11 shows BER as a function of the carrier frequency under different atmospheric attenuation conditions, gas, cloud/fog, and rain. The top row with Figure 11(a1)–11(c1) represents the BER associated with gas, clouds/fog, and rain, respectively, under mild conditions; whereas the bottom row with Figure 11(a2)–(c2) represents the respective BER under inclement conditions. For all the simulations, the BER threshold for performance evaluation is set to 1%. The values of distance d , height h , ambient temperature T_a , ambient pressure p_a , power transmission P_{tx} , and channel bandwidth B_{ch} are 2000 m, 400 m, 25 °C, 1013.25 hPa, 75 mW, and 20 MHz, respectively, for all six cases. The mild and inclement weather conditions for each category of gas, clouds/fog, and rain are differentiated by the values used for water vapor density (wvd), liquid water density (lwd), and rain rate R_r , respectively. For each of the six cases, five modulation schemes, viz., BPSK, QPSK, 16-QAM, 64-QAM, and 256-QAM, are evaluated for their BER performance.

The point of intersection between the 1% reference BER line and the BER curve associated with a particular modulation scheme indicates the respective maximum operating frequency f_{max} . In other words, f_{max} for a given modulation scheme is the maximum permissible operating frequency for which the BER does not exceed the threshold.

Figure 11(a1) illustrates the BER performance as a function of the frequency in the presence of gas attenuation under mild conditions, represented by a water vapor density of 0.23 g/m^3 , which in turn corresponds to 1% relative humidity. This condition represents extremely dry air conditions and, as such, the attenuation due to atmospheric gases is minimum. The f_{max} for each modulation scheme is at its absolute maximum value in this case. For reference, f_{max} for BPSK/QPSK is marked by a green crosshair in this plot.

Figure 11(a2) shows the BER performance for the assumed modulation schemes under inclement weather conditions for atmospheric gases. In this case, 100% relative humidity is assumed, which translates to 23.01 g/m^3 of water vapor density. Compared to the

mild weather conditions, operating bandwidth reduction, B_{red} , of 1 MHz resulted for BPSK/QPSK.

Figure 11(b1) depicts the BER performance for the assumed modulation schemes under mild cloud/fog conditions, represented by a liquid water density (lwd) of 0.05 g/m^3 , yielding a visibility of 300 m.

Figure 11(b2) illustrates the BER performance under corresponding inclement cloud/fog conditions. In this case, lwd of 10 g/m^3 , corresponding to a visibility of 5 m, is assumed. This represents extremely thick cloud/fog conditions. In comparison to the mild cloud/fog conditions, a B_{red} of 295 MHz resulted in this case. The substantial increase in B_{red} is attributable to the increased attenuation caused by inclement cloud/fog conditions.

Figure 11(c1) presents the BER performance under mild rain conditions, utilizing a rain rate R_r of 1 mm/h under the specified condition. In comparison to the operating bandwidth observed under mild gases and cloud/fog conditions, mild rain results in a reduction of the operating bandwidth by 8 MHz and 2 MHz for BPSK and QPSK based operations, respectively.

Figure 11(c2) illustrates the case of extremely heavy rain using R_r of 120 mm/h. As expected, due to a significant increase in attenuation, f_{max} for BPSK/QPSK is significantly reduced, yielding a B_{red} of 2075 MHz.

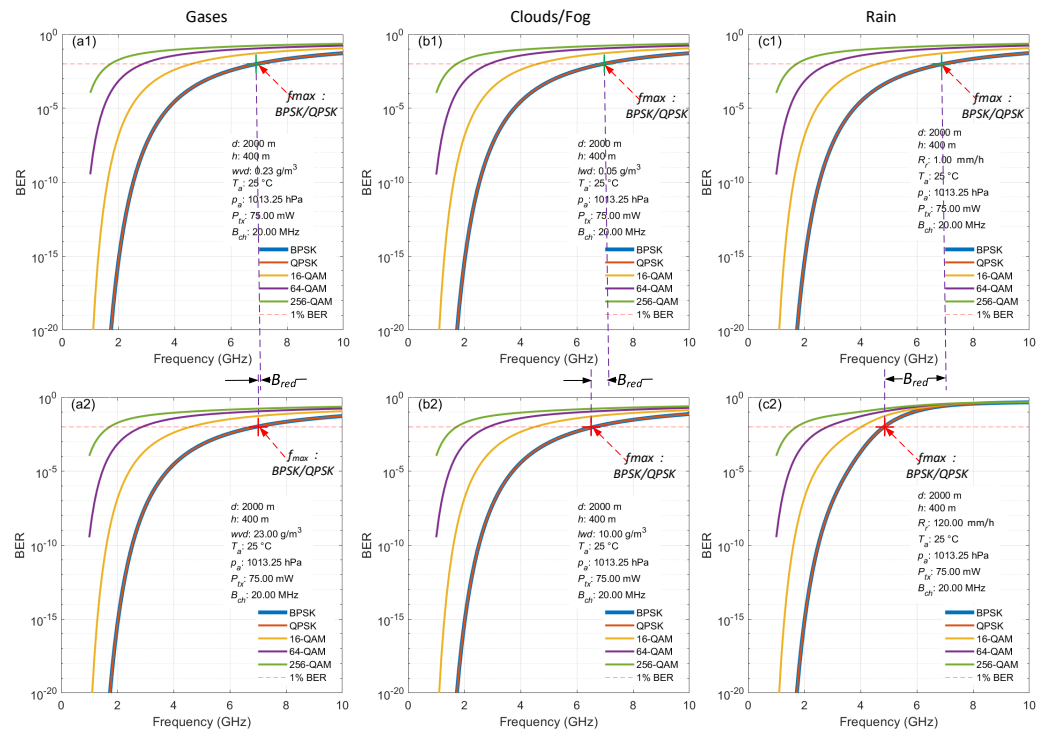


Figure 11. BER as a function of frequency for gas, cloud/fog, and rain-based attenuation. Top row (a1–c1) represents BER resulting from attenuations due to gas, cloud/fog, and rain, respectively, with atmospheric parameter values causing relatively lesser attenuation. Bottom row (a2–c2) represents BER resulting from attenuation due to gas, cloud/fog, and rain, respectively, with atmospheric parameter values causing higher attenuation, resulting in reduction of operating bandwidth.

Sensitivity of the bit error rate to the modulation scheme is shown by the results. The BER increases as more and more symbols are accommodated in the symbol constellation using a higher order modulation scheme. This occurs due to the reduced error vector margins between symbols when employing higher-order modulation schemes. Because of the reduced error vector margin, the symbol decision boundary is crossed even under reduced interference, reduced SNR, and Doppler shift. Since Doppler shift is inseparably

connected with UAV operations due to their mobility, the connection between the bit error rate and the modulation scheme is very significant. As the simplest measure, bit error rate could be mitigated by switching to a lower order modulation, which leads to increased separation between the symbols in the constellation space.

In summary, as the atmospheric weather conditions deteriorate, the SNR degrades due to the increase in resultant attenuation. This degradation is mitigated by a corresponding reduction in operating frequency. At lower operating frequencies, the free space path loss decreases, and, with this reduction, the received signal energy improves at the receiver, thereby enhancing the SNR. The value of f_{max} decreases as well, resulting in operating bandwidth reduction, or bandwidth suboptimization.

Our analysis on the impact of inclement weather conditions on UAV operations is command and control communication centered. While it provides a detailed insight into the bandwidth suboptimization, it does not consider other aspects of UAV operations under inclement weather conditions. For example, under dense clouds/fog, due to impairment of visibility, UAVs needing constant visibility by the operator may not be operable. Similarly, under rainy conditions, the operations of UAVs are subject to required protection from water for fail-proof operation of the onboard electronics.

As rain is the most severe factor affecting UAV operations, suitable mitigation techniques could be used to permit UAV operation under severe rain conditions. A water-resistant mechanical design would protect the on-board circuitry against precipitation. Signal attenuation under severe rainfall and the consequent communication reliability could be addressed through the implementation of diversity schemes, such as a multiple input, multiple output (MIMO) radio front-end. Furthermore, communication reliability could be enhanced by improving the signal-to-noise ratio through increased power transmission and/or reduced operating frequency and modulation order.

Table 4 presents the results of f_{max} and B_{red} for the specified modulation schemes and weather conditions under two distinct power transmissions, 25 mW and 75 mW. For each power transmission, the corresponding f_{max} and B_{red} values are provided for both mild and inclement weather conditions. The light orange color fonts are used for convenient differentiation of the three attenuation factors: gases, clouds/fog, and rain. This same color scheme applies to the associated atmospheric variable that primarily affects the attenuation. The right pointing arrow implies the associated values assumed by the corresponding atmospheric variables for the light and inclement weather conditions.

With two distinct power transmissions and two separate weather conditions, a total of four combinations of power and weather conditions are created. These combinations are marked as—(a) low power and mild weather (LPMW), (b) low power and inclement weather (LPIW), (c) high power and mild weather (HPMW), and (d) high power and inclement weather (HPIW). The f_{max} for various modulation schemes are shown in the f_{max_LPMW} , f_{max_LPIW} , f_{max_HPMW} , and f_{max_HPIW} columns. The bandwidth reduction in MHz is shown in the B_{red_LP} and B_{red_HP} columns corresponding to the low and high-power modes, respectively.

Given that both free-space path loss and weather-induced attenuation decrease at lower frequencies, maintaining the required SNR for a specified BER threshold necessitates a reduction in operating frequency when the power transmission decreases or weather conditions deteriorate. Consequently, the LPIW condition results in having the lowest values for f_{max} . Conversely, an increase in power transmission and the presence of favorable weather conditions result in higher f_{max} attainment, as the increased path loss due to the utilization of higher operating frequency is mitigated by the elevated power transmission and reduced attenuation associated with mild weather conditions. As such, the HPMW condition results in having the highest values for f_{max} .

Table 4. Comparison of f_{max} and B_{red} under different power transmissions.

Atmospheric Attenuation Factors (↓)	Modulation (↓)	$P_{tx}:25\text{ mW}$			$P_{tx}:75\text{ mW}$		
		LPMW f_{max_LPMW} (GHz)	LPIW f_{max_LPIW} (GHz)	B_{red_LP} (MHz)	HPMW f_{max_HPMW} (GHz)	HPIW f_{max_HPIW} (GHz)	B_{red_HP} (MHz)
Gases	$wvd \rightarrow$	0.23 (g/m ³)	23.01 (g/m ³)		0.23 (g/m ³)	23.01 (g/m ³)	
	BPSK/QPSK	4.000	4.000	0	6.901	6.900	1
	16-QAM	2.636	2.636	0	4.556	4.555	1
	64-QAM	1.636	1.636	0	2.895	2.895	0
	256-QAM	1.000	1.000	0	1.727	1.727	0
Clouds/Fog	$lwd \rightarrow$	0.05 (g/m ³)	10 (g/m ³)		0.05 (g/m ³)	10 (g/m ³)	
	BPSK/QPSK	4.000	4.000	0	6.895	6.600	295
	16-QAM	2.636	2.636	0	4.558	4.505	53
	64-QAM	1.636	1.636	0	2.895	2.858	37
	256-QAM	1.000	1.000	0	1.727	1.727	0
Rain	$R_r \rightarrow$	1 (mm/h)	120 (mm/h)		1 (mm/h)	120 (mm/h)	
	BPSK/QPSK	4.000	3.636	364	6.893	4.818	2075
	16-QAM	2.636	2.633	3	4.557	3.885	672
	64-QAM	1.636	1.635	1	2.894	2.818	76
	256-QAM	1.000	1.000	0	1.726	1.725	1

d : 2000 m, h : 400 m, T_a : 25 °C, p_a : 1013.25 hPa, B_{ch} : 20 MHz.

It can be observed in Table 4 that B_{red} is minimally affected at lower power transmissions. This is attributable to the fact that, at lower power transmissions, the corresponding f_{max} is inherently smaller, and as weather conditions deteriorate, the increase in attenuation is comparatively smaller. The noise power remains constant due to the fixed temperature and operating bandwidth, resulting in a relatively smaller reduction in SNR. Consequently, no discernible difference in B_{red} is observed for the gases and cloud/fog-influenced weather conditions at the assumed lower power transmission. The highest B_{red_LP} of 364 MHz is observed in association with rain for BPSK and QPSK. The B_{red} decreases substantially to 3 MHz and 1 MHz for 16-QAM and 64-QAM, respectively. No changes in f_{max} are observed for 256-QAM, making the corresponding B_{red} equal to zero.

By contrast, B_{red} exhibits maximum susceptibility at higher power transmissions, as a greater value of associated f_{max} results in significant atmospheric attenuation under deteriorating weather conditions. With noise power remaining constant, this phenomenon leads to a more substantial degradation of SNR, consequently necessitating a larger reduction in f_{max} , and ultimately resulting in maximum B_{red} . A bandwidth reduction of 1 MHz is observed for BPSK/QPSK and 16-QAM under gas-based inclement weather conditions, while the operating bandwidth remains unaffected for 64-QAM and 256-QAM due to their lower f_{max} . In the presence of cloud/fog-based inclement weather conditions, higher atmospheric attenuation results in a greater reduction in f_{max} , consequently leading to a more substantial B_{red} . Specifically, for BPSK/QPSK, 16-QAM, and 64-QAM, B_{red} values of 295 MHz, 53 MHz, and 37 MHz are observed, respectively. Inclement rainy conditions result in maximum B_{red} due to the highest atmospheric attenuation. For BPSK/QPSK, 16-QAM, 64-QAM, and 256-QAM the B_{red} values are 2075 MHz, 672 MHz, 76 MHz, and 1 MHz, respectively.

Currently available UAVs' operations are based in the <10 GHz bands. Accordingly, our simulation for BER is for the frequency region of 1 to 10 GHz. Splitting this band in lower and higher regions, the lower bandwidth regions correspond to frequencies below 5 GHz.

Our results demonstrate that, at a lower bandwidth corresponding to the lower frequency region (<5 GHz), the BER remains below the threshold of 1% for all modulation schemes and weather conditions considered. As attenuation decreases with a reduction in frequency, for UAVs operating at frequencies <1 GHz, the BER is anticipated to improve, resulting in enhanced communication reliability. Hence, for lower UAV operations in lower frequency regions and occupying smaller bandwidths, no explicit evaluation of BER is needed.

In brief, the key insights can be summarized as follows:

- f_{max} tends to reduce with reduction in power transmission and worsening of weather conditions
- f_{max} tends to increase with the increase in power transmission and weather conditions becoming milder
- At lower power transmissions, inclement weather conditions cause minimum bandwidth reduction
- At higher power transmissions, inclement weather conditions result in maximum bandwidth reduction
- Higher bandwidth reduction is seen with a lower order modulation scheme
- Lower bandwidth reduction is seen with a higher order modulation scheme

These observations, as seen in our simulation-based studies, are apt for algorithmic development to dynamically control the operating frequencies in UAV operations.

Figure 12 is another representation of the results given in Table 4. It shows the variations in maximum operating frequency and bandwidth reduction resulting from alterations in meteorological conditions under distinct power transmissions and modulation schemes. The columns marked (a) and (b) represent the power transmissions of 25 mW and 75 mW, respectively. The plots in the top, middle, and bottom rows correspond to gases, clouds/fog, and rain-based attenuation and resulting f_{max} and B_{red} for various modulation schemes, respectively.

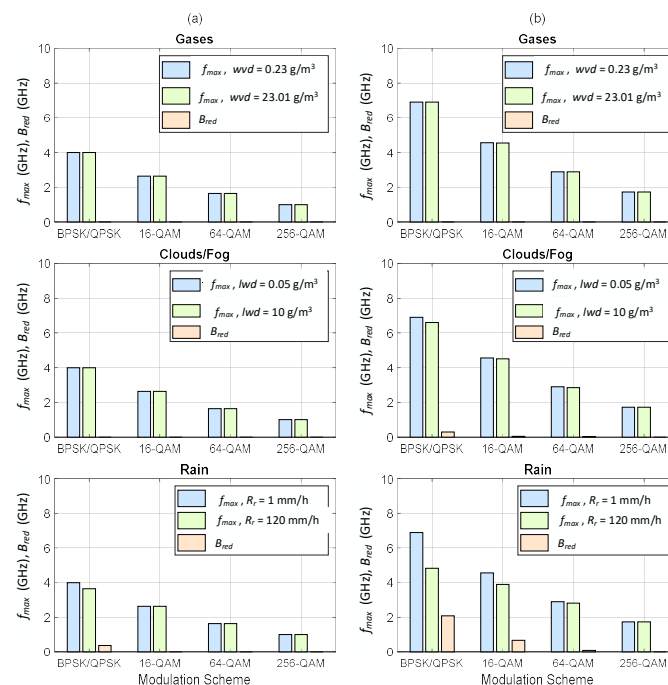


Figure 12. Variations in maximum operating frequency and bandwidth reduction resulting from alterations in meteorological conditions under distinct power transmissions and modulation schemes. Figures in column (a) depict the results for a power transmission of 25 mW. Figures in column (b) illustrate the results for a power transmission of 75 mW. For all scenarios, distance and height are 2000 m and 400 m, respectively.

Algorithm 1 depicts the procedure to determine f_{max} using an exemplary set of parameters, and path loss model.

Algorithm 1. Example determination of new f_{max} under varying weather conditions

Maximum Operating Frequency Calculation for BER = 0.01

```

1: Input:
2:  $P_t = 0.025$  W ▷ Transmit power
3:  $d = 2000$  m ▷ Distance between transmitter and receiver
4:  $f_{min} = 1$  GHz,  $f_{max} = 100$  GHz ▷ Frequency range
5:  $B = 1$  MHz ▷ Bandwidth
6:  $T = 290$  K ▷ Temperature
7:  $BER_{target} = 0.01$  ▷ Target BER
8: Constants:
9:  $c = 3 \times 10^8$  m/s ▷ Speed of light
10:  $k = 1.38 \times 10^{-23}$  J/K ▷ Boltzmann's constant
11: Initialize:
12:  $N_0 = k \times T$  ▷ Noise spectral density
13:  $f_{operating} = 0$  GHz ▷ Variable to store the maximum operating frequency
14: Step 1: Compute noise power
15:  $P_{noise} = N_0 \times B$ 
16: Step 2: Frequency loop from  $f_{min}$  to  $f_{max}$ 
17: for each frequency  $f$  from  $f_{min}$  to  $f_{max}$  do
18:   a. Compute free-space path loss  $L_p(f)$ 
19:    $L_p(f) = \left(\frac{4\pi df}{c}\right)^2$ 
20:   b. Compute atmospheric attenuation  $L_{atm}(f)$ 
21:    $L_{atm}(f) = 10^{-\frac{\alpha(f) \cdot d}{10}}$ 
22:   c. Compute total path loss  $L_{total}(f)$ 
23:    $L_{total}(f) = L_p(f) \cdot L_{atm}(f)$ 
24:   d. Compute received power  $P_r(f)$ 
25:    $P_r(f) = \frac{P_t}{L_{total}(f)}$ 
26:   e. Compute signal-to-noise ratio (SNR)
27:    $SNR(f) = \frac{P_r(f)}{P_{noise}}$ 
28:   f. Compute BER for 16-QAM modulation scheme
29:    $BER(f) = \frac{4}{\log_2(M)} Q\left(\sqrt{\frac{3 \cdot SNR(f)}{M-1}}\right)$ 
▷ Assume  $M = 16$  for 16-QAM
30:
31:   g. Check if  $BER(f) \leq BER_{target}$ 
32:   if  $BER(f) \leq BER_{target}$  then
33:      $f_{operating} = f$  ▷ Update maximum operating frequency
34:   end if
35: end for
36: Step 3: Output  $f_{operating}$ 
37: return  $f_{operating}$  ▷ Maximum frequency that meets  $BER \leq 0.01$ 

```

3.2. Mobility and Doppler Shift

Using the previously derived model for effective SNR (ψ), and the defined parameters, we simulated the effect of relative speed variations for different values of sub-carrier spacing, number of sub-carriers, and QAM modulation orders.

Figure 13 illustrates effective SNR, after degradation to a reference SNR of 20 dB, and carrier frequency of 2.4 GHz, induced by Doppler shift within a velocity range of 0 to 200 km/h, for four distinct symbol rates of 15, 30, 60, and 120 Kbd/s, represented by Figure 13a–d, respectively. In all four figures, the solid color lines in blue, orange, yellow,

purple, and green correspond to sub-carrier quantities of 4, 16, 32, 64, and 256, respectively. While the dotted horizontal lines in blue, orange, yellow, and green correspond to the minimum SNR threshold to maintain a BER of 0.01 for QAM modulation orders of 4, 16, 32, 64, and 256, respectively. Due to fixed carrier frequency of 2.4 GHz, with respect to the relative motion, the same Doppler shift variation applies to all four cases.

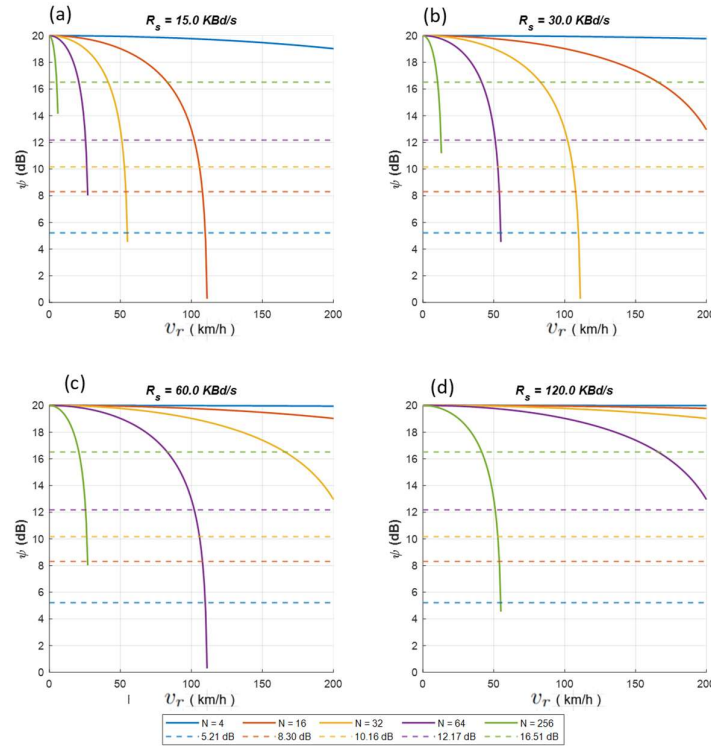


Figure 13. Illustration of SNR degradation caused by Doppler shift at carrier frequency of 2.4 GHz, and for four distinct symbol rates (R_s): (a) illustrates SNR degradation for R_s of 15 KBd/s; (b) depicts SNR degradation for R_s of 30 KBd/s; (c) elucidates SNR degradation for R_s of 60 KBd/s; and (d) elucidates SNR degradation for R_s of 120 KBd/s. In each figure, SNR degradations for the number of sub-carriers (N) corresponding to 4, 16, 32, 64, and 256 are represented by blue, red, orange, purple, and green solid lines, respectively. Dotted horizontal lines in blue, red, orange, yellow, purple, and green correspond to the minimum required SNR threshold (in dB) to yield a BER of 0.01 for QAM modulation order (M) of 4, 16, 32, 64, and 256, respectively. The reference static channel-based SNR against which degradation is computed is fixed at 20 dB.

Figure 13a depicts the degradation for the fixed symbol rate (R_s) of 15 KBd/s. In this case, the fastest degradation of SNR is observed. This is due to the higher ICI noise power applied to a narrower bandwidth for a given number of sub-carrier N . The reason for a narrower bandwidth per sub-carrier is a relatively smaller symbol rate, that makes the symbol duration longer in the time domain but narrower in the frequency domain.

In this case, for a sub-carrier count of $N = 4$, the SNR threshold for the maximum BER is not reached for any combination of speed and modulation order and, hence, reliable operation is possible under all conditions. For $N = 16$, the SNR threshold for 4, 16, 32, 64, and 256-QAM is reached at 110, 108, 105, 102, and 82 km/h, respectively. As the number of sub-carriers increases with $N = 32$, the maximum permissible relative speed reduces to 55, 54, 53, 51, and 40 km/h for 4, 16, 32, 64, and 256-QAM, respectively. This trend continues and, as the number of sub-carriers increases, the range of maximum permissible relative speed decreases. Specifically, with $N = 64$, the maximum operating speed drops to 27 km/h, while for $N = 256$ operation is not possible beyond a speed of 5 km/h.

Figure 13b shows the degradation corresponding to symbol rate of 30 KBd/s. In this case, due to doubling of the sub-carrier spacing, twice as much bandwidth is occupied in comparison to the symbol rate of 15 KBd/s. The net effect is a reduction in SNR degradation and a corresponding increase in operating speed ranges for all cases of sub-carrier count N and modulation schemes. With doubling of the sub-carrier spacing, the corresponding Doppler speed range also doubled.

The trend of operating Doppler speed range doubling with corresponding doubling of the symbol rate, and hence sub-carrier spacing, is also seen for cases as depicted in Figure 13c,d. This can also be explained by the presence of the term $\left(\pi N \frac{v_r f_c}{R_s c}\right)^2$ in Equation (16) that governs SNR degradation. As R_s is multiplied by a constant, to maintain the same value for the above governing term from Equation (16), v_r must be multiplied by the same constant. Other behavior, such as increased SNR degradation with the increase in N , can also be explained on purely mathematical ground using the above governing term.

In summary, the results show that relative motion caused Doppler shift is a major cause of SNR degradation in UAV communication. SNR degradation could be minimized by following several approaches. While speed reduction is one obvious choice, it may not be possible under all circumstances. To mitigate the effect of an increase in relative speed by a factor of k , one of the following rudimentary approaches could be followed:

- Decrease the carrier frequency f_c by a factor of k
- Increase the symbol rate R_s by a factor of k
- Decrease the number of sub-carrier N by a factor p : $\frac{N}{p} \in \mathbb{Z}^+$ and $\frac{k}{p} \leq 1$.

4. Conclusions

In this work, we examined the impact of atmospheric conditions, specifically atmospheric gases, clouds, fog, and rain, on bandwidth availability, utilizing signal attenuation and bit error rate across five different modulation schemes, employing weather conditions pertinent to UAV operations. Our findings revealed that atmospheric attenuation increases with both propagation distance and frequency, and precipitation further amplifies this effect. Temperature and pressure variations were found to have a minimal impact on attenuation over short distances. The analysis highlighted that the principal parameters influencing atmospheric attenuation are distance, frequency, and precipitation, resulting in an elevated BER. In the lower frequency (<10 GHz) bands, where currently available UAVs operate, a comparative analysis of the impact of atmospheric gases, clouds, fog, and rain on attenuation reveals that atmospheric gases have the least effect on short-range UAV command and control communications bandwidth. Although clouds and fog contribute to attenuation to a greater extent than gases, their impact is relatively minor in comparison to rain, which significantly affects attenuation due to the larger size of raindrops, resulting in increased scattering and absorption. While lower-order modulation schemes and higher power transmissions result in an increase of maximum operating frequency, a decrease in the same is observed with the reduction of power transmission and utilization of higher-order modulation schemes. Given that the attenuation increases with frequency, the utilization of higher operating frequencies, supported by higher operating power levels and lower-order modulation schemes, results in more pronounced bandwidth suboptimization under adverse weather conditions. The complex interaction between the power transmission, modulation-order, and weather conditions in influencing the maximum operating frequency represents a significant finding in our research, with potential applications in the development of spectrum management algorithms for UAV operation. The key takeaway message for UAV operators is that inclement weather conditions and Doppler shift degrade UAV link performance and mitigation is possible using a variety of options, such as using low carrier frequencies, low modulation orders, and low speeds. For link

budgeting purposes, at least 50 dB additional path loss should be included. Low frequency bands should be reserved for critical command and communications. Also, for UAV link operation, higher symbol rates should be supported at low carrier frequencies.

Author Contributions: Conceptualization, simulation, and original draft writing, L.M., organization, supervision, and thorough review, N.K. All authors have read and agreed to the published version of the manuscript.

Funding: This research was funded by National Aeronautics and Space Administration (NASA) under award No. 08708.

Data Availability Statement: The original contributions presented in this study are included in the article. Further inquiries can be directed to the corresponding authors.

Acknowledgments: This paper is based on work supported by National Aeronautics and Space Administration (NASA) under award No. 08708. Any opinions, findings, conclusions, or recommendations expressed in this material are those of the author(s) and do not necessarily reflect the view of NASA. The authors extend their appreciation to the anonymous reviewers whose constructive feedback has contributed to the enhancement of this manuscript significantly.

Conflicts of Interest: The authors declare no conflict of interest.

References

1. Butilă, E.V.; Boboc, R.G. Urban Traffic Monitoring and Analysis Using Unmanned Aerial Vehicles (UAVs): A Systematic Literature Review. *Remote Sens.* **2022**, *14*, 620. [[CrossRef](#)]
2. Muñoz, J.; López, B.; Quevedo, F.; Monje, C.A.; Garrido, S.; Moreno, L.E. Multi Uav Coverage Path Planning in Urban Environments. *Sensors* **2021**, *21*, 7365. [[CrossRef](#)] [[PubMed](#)]
3. Song, M.; Huo, Y.; Liang, Z.; Dong, X.; Lu, T. UAV Communication Recovery under Meteorological Conditions. *Drones* **2023**, *7*, 423. [[CrossRef](#)]
4. Song, M.; Huo, Y.; Lu, T.; Dong, X.; Liang, Z. Meteorologically Introduced Impacts on Aerial Channels and UAV Communications. In Proceedings of the IEEE Vehicular Technology Conference, Victoria, BC, Canada, 18 November–16 December 2020.
5. Thibbotuwawa, A.; Bocewicz, G.; Radzki, G.; Nielsen, P.; Banaszak, Z. UAV Mission Planning Resistant to Weather Uncertainty. *Sensors* **2020**, *20*, 515. [[CrossRef](#)] [[PubMed](#)]
6. ITU-R. Recommendation ITU-R P.676-12—Attenuation by Atmospheric Gases and Related Effects; ITU-R: Geneva, Switzerland, 2019.
7. ITU-R. Recommendation ITU-R P.840-9—Attenuation Due to Clouds and Fog; ITU-R: Geneva, Switzerland, 2023.
8. ITU-R. Recommendation ITU-R P.838-3 Specific Attenuation Model for Rain for Use in Prediction Methods; ITU-R: Geneva, Switzerland, 2005.
9. Zang, S.; Ding, M.; Smith, D.; Tyler, P.; Rakotoarivelo, T.; Kaafar, M.A. The Impact of Adverse Weather Conditions on Autonomous Vehicles: How Rain, Snow, Fog, and Hail Affect the Performance of a Self-Driving Car. *IEEE Veh. Technol. Mag.* **2019**, *14*, 103–111. [[CrossRef](#)]
10. Modeling, A.C. Atmospheric Parameters Influence on Mm-Wave Propagation in 5G Communication. In Proceedings of the 2019 7th Mediterranean Congress of Telecommunications (CMT), Fez, Morocco, 24–25 October 2019; pp. 1–5.
11. Tashan, W.; Shayea, I.; Aldirmaz-Colak, S.; Rahman, T.A.; El-Saleh, A.A.; Roslee, M. Rain Rate and Rain Attenuation Over Millimeter Waves in Tropical Regions Based on Real Measurements. In Proceedings of the 15th IEEE Malaysia International Conference on Communications: Emerging Technologies in IoT and 5G, MICC 2021—Proceedings, Virtual, 1–2 December 2021; Institute of Electrical and Electronics Engineers Inc.: Piscataway, NJ, USA, 2021; pp. 120–125.
12. Golovachev, Y.; Pinhasi, G.A.; Pinhasi, Y. Atmospheric Effects on Ofdm Wireless Links Operating in the Millimeter Wave Regime. *Electronics* **2020**, *9*, 1598. [[CrossRef](#)]
13. Weng, Z.K.; Kanno, A.; Dat, P.T.; Inagaki, K.; Tanabe, K.; Sasaki, E.; Kurner, T.; Jung, B.K.; Kawanishi, T. Millimeter-Wave and Terahertz Fixed Wireless Link Budget Evaluation for Extreme Weather Conditions. *IEEE Access* **2021**, *9*, 163476–163491. [[CrossRef](#)]
14. Mankong, U.; Chamsuk, P.; Nakprasert, S.; Potha, S.; Weng, Z.K.; Dat, P.T.; Kanno, A.; Kawanishi, T. Millimeter Wave Attenuation Due to Wind and Heavy Rain in a Tropical Region. *Sensors* **2023**, *23*, 2532. [[CrossRef](#)] [[PubMed](#)]
15. Yilmaz, A.; Yilmaz, N.; Kalem, G.; Durmaz, M.A. Path Gain and Channel Capacity for HAP-to-HAP Communications. In Proceedings of the 2023 International Conference on Unmanned Aircraft Systems, ICUAS 2023, Warsaw, Poland, 6–9 June 2023; Institute of Electrical and Electronics Engineers Inc.: Piscataway, NJ, USA, 2023; pp. 305–312.

16. Al-Gburi, A.; Abdullah, O.; Sarhan, A.Y.; Al-Hraishawi, H. Channel Estimation for UAV Communication Systems Using Deep Neural Networks. *Drones* **2022**, *6*, 326. [CrossRef]
17. Zhang, Z.; Liu, Y.; Huang, J.; Zhang, J.; Li, J.; He, R. Channel Characterization and Modeling for 6G UAV-Assisted Emergency Communications in Complicated Mountainous Scenarios. *Sensors* **2023**, *23*, 4998. [CrossRef] [PubMed]
18. The Atmosphere | National Oceanic and Atmospheric Administration. Available online: <https://www.noaa.gov/jetstream/atmosphere> (accessed on 5 November 2024).
19. Golovachev, Y.; Etinger, A.; Pinhasi, G.A.; Pinhasi, Y. Propagation Properties of Sub-Millimeter Waves in Foggy Conditions. *J. Appl. Phys.* **2019**, *125*, 151612. [CrossRef]
20. Mao, T.-P.; Zhou, D.-F.; Niu, Z.-X. The Calculation Model of the Attenuation Due to Clouds or Fog and the Analysis of Its Characteristic. In Proceedings of the 2004 Asia-Pacific Radio Science Conference, Qingdao, China, 24–27 August 2004; Proceedings; IEEE: Piscataway, NJ, USA, 2004; pp. 332–334.
21. Goldsmith, A. *Wireless Communications*; Cambridge University Press: Cambridge, UK, 2005; ISBN 9780521837163.
22. Supramongkonset, J.; Duangsuwan, S.; Maw, M.M.; Promwong, S. Empirical Path Loss Channel Characterization Based on Air-to-Air Ground Reflection Channel Modeling for UAV-Enabled Wireless Communications. *Wirel. Commun. Mob. Comput.* **2021**, *2021*, 5589487. [CrossRef]
23. Zhou, L.; Ma, H.; Yang, Z.; Zhou, S.; Zhang, W. Unmanned Aerial Vehicle Communications: Path-Loss Modeling and Evaluation. *IEEE Veh. Technol. Mag.* **2020**, *15*, 121–128. [CrossRef]
24. Cheng, X.; Li, Y.; Bai, L. UAV Communication Channel Measurement, Modeling, and Application. *J. Commun. Inf. Netw.* **2019**, *4*, 32–43. [CrossRef]
25. Su, Z.; Li, C.; Chen, W. A Non-Stationary Cluster-Based Channel Model for Low-Altitude Unmanned-Aerial-Vehicle-to-Vehicle Communications. *Drones* **2023**, *7*, 640. [CrossRef]
26. Pollet, T.; Van Bladel, M.; Moeneclaey, M. BER Sensitivity of OFDM Systems to Carrier Frequency Offset and Wiener Phase Noise. *IEEE Trans. Commun.* **1995**, *43*, 191–193. [CrossRef]
27. Bithas, P.S.; Nikolaidis, V.; Kanas, A.G.; Karagiannidis, G.K. UAV-to-Ground Communications: Channel Modeling and UAV Selection. *IEEE Trans. Commun.* **2020**, *68*, 5135–5144. [CrossRef]
28. Jie Seah, S.; Leow, C.Y.; Nalingsam, R.; Kiat New, W.; Alam, R.; Ling Jong, S.; Yin Lam, H.; Almasoud, A.M. Empirical Channel Models for UAV Communication: A Comparative Study. *IEEE Access* **2024**, *12*, 96740–96756. [CrossRef]
29. Cui, Z.; Guan, K.; Briso-Rodríguez, C.; Ai, B.; Zhong, Z.; Oestges, C. Channel Modeling for UAV Communications: State of the Art, Case Studies, and Future Directions. *arXiv* **2020**, arXiv:2012.06707.
30. Robertson, P.; Kaiser, S. The Effects of Doppler Spreads in OFDM(A) Mobile Radio Systems. In Proceedings of the Gateway to 21st Century Communications Village. VTC 1999-Fall. IEEE VTS 50th Vehicular Technology Conference (Cat. No.99CH36324), Amsterdam, The Netherlands, 19–22 September 1999.
31. Xiong, F. *The Effect of Doppler Frequency Shift, Frequency Offset of the Local Oscillators, and Phase Noise on the Performance of Coherent OFDM Receivers*; NASA: Washington, DC, USA, 2001.
32. 2023 Was Earth's Hottest Year on Record. Yale Climate Connections. Available online: <https://yaleclimateconnections.org/2024/01/2023-was-earths-hottest-year-on-record/> (accessed on 3 December 2024).
33. Mavic Mini User Manual v1.0 | Shenzhen DJI Sciences and Technologies Ltd. Available online: https://dl.djicdn.com/downloads/Mavic_Mini/Mavic_Mini_User_Manual_v1.0_en_1.pdf (accessed on 7 November 2024).
34. Garcia-Corrales, C.; Martin-Vega, F.J.; Lopez-Martinez, F.J.; Canete, F.J.; Paris, J.F. Understanding the Impact of Line-of-Sight in the Ergodic Spectral Efficiency of Cellular Networks. In Proceedings of the 2018 IEEE 23rd International Workshop on Computer Aided Modeling and Design of Communication Links and Networks (CAMAD), Barcelona, Spain, 17–19 September 2018; IEEE: Piscataway, NJ, USA, 2018; ISBN 9781538661512.
35. TSGR TR 138 901-V16.1.0-5G; Study on Channel Model for Frequencies from 0.5 to 100 GHz (3GPP TR 38.901 Version 16.1.0 Release 16); ETSI: Sophia Antipolis, France, 2020.
36. Huang, J.; Cao, Y.; Raimundo, X.; Cheema, A.; Salous, S. Rain Statistics Investigation and Rain Attenuation Modeling for Millimeter Wave Short-Range Fixed Links. *IEEE Access* **2019**, *7*, 156110–156120. [CrossRef]
37. Alozie, E.; Abdulkarim, A.; Abdullahi, I.; Usman, A.D.; Faruk, N.; Olayinka, I.F.Y.; Adewole, K.S.; Oloyede, A.A.; Chiroma, H.; Sowande, O.A.; et al. A Review on Rain Signal Attenuation Modeling, Analysis and Validation Techniques: Advances, Challenges and Future Direction. *Sustainability* **2022**, *14*, 11744. [CrossRef]
38. Han, C.; Feng, L.; Huo, J.; Deng, Z.; Zhang, G.; Ji, B.; Zhou, Y.; Bi, Y.; Duan, S.; Yuan, R. Characteristics of Rain-Induced Attenuation over Signal Links at Frequency Ranges of 25 and 38 Ghz Observed in Beijing. *Remote Sens.* **2021**, *13*, 2156. [CrossRef]

Disclaimer/Publisher's Note: The statements, opinions and data contained in all publications are solely those of the individual author(s) and contributor(s) and not of MDPI and/or the editor(s). MDPI and/or the editor(s) disclaim responsibility for any injury to people or property resulting from any ideas, methods, instructions or products referred to in the content.